Thin Solid Films, *518 (2010) 4791–4797; doi:10.1016/j.tsf.2010.01.037*.

Thin Film Deposition and Characterization of Pure and Iron-Doped Electron-Beam Evaporated Tungsten Oxide for Gas Sensors

[a]*Tuquabo Tesfamichael, [b]Masashi Arita, [c]Thor Bostrom, [d]John Bell,

[a] Faculty of Built Environment and Engineering, School of Engineering Systems

[c] Faculty of Science, Analytical Electron Microscopy Facility

[d] Centre for Built Environment and Engineering Research

Queensland University of Technology, 2 George Street,

Brisbane, QLD 4000, Australia

[b] Graduate School of Information Science and Technology, Hokkaido University, Kita-14, Nishi-9, Kita-ku, Sapporo, 060-0814, Japan

***Corresponding author**: Dr T. Tesfamichael, Phone: +61738641988, Fax:+61738641516, email: t.tesfamichael@qut.edu.au

Abstract

Pure Tungsten Oxide (WO_3) and Iron-doped (10 at%) Tungsten Oxide (WO_3:Fe) nanostructured thin films were prepared using a dual crucible Electron Beam Evaporation techniques. The films were deposited at room temperature in high vacuum condition on glass substrate and post-heat treated at 300 ^oC for 1 hour. From the study of X-ray diffraction and Raman the characteristics of the as-deposited WO_3 and WO_3:Fe films indicated non-crystalline nature. The surface roughness of all the films showed in the order of 2.5 nm as observed using Atomic Force Microscopy (AFM). X-Ray Photoelectron

Thin Solid Films, *518 (2010) 4791–4797; doi:10.1016/j.tsf.2010.01.037*.

Spectroscopy (XPS) analysis revealed tungsten oxide films with stoichiometry close to WO_3. The addition of Fe to WO_3 produced a smaller particle size and lower porosity as observed using Transmission Electron Microscopy (TEM). A slight difference in optical band gap energies of 3.22 eV and 3.12 eV were found between the as-deposited WO_3 and WO_3:Fe films, respectively. However, the difference in the band gap energies of the annealed films were significantly higher having values of 3.12 eV and 2.61 eV for the WO_3 and WO_3:Fe films, respectively. The heat treated samples were investigated for gas sensing applications using noise spectroscopy and doping of Fe to WO_3 reduced the sensitivity to certain gasses. Detailed study of the WO_3 and WO_3:Fe films gas sensing properties is the subject of another paper.

Keywords: Iron-doped Tungsten oxide; Electron beam evaporation; Co-evaporated thin films; Surface morphology; Optical properties; Surface characterization

1. Introduction

Various techniques have been used to deposit metal oxide thin films for gas sensing applications. This includes sol-gel, chemical vapor deposition, advanced gas deposition, and physical vapor deposition [1-6]. Each of the film deposition techniques has its own advantages and limitations. The gas sensing properties of the metal oxides are determined by their intrinsic properties, but can also be enhanced by adding impurities, reducing particle size, and modifying the surface morphology and porosity of the films. Thin films are usually compact and the sensing layer is limited to the surface whereas thicker films are commonly porous and hence the whole layer can interact with the gas species. If a controlled porosity can be achieved, then the gas sensing properties of nanostructured thin

films can be enhanced significantly [7]. From a theoretical study elsewhere, the sensitivity for gas detection can be improved if the grain size is smaller than 50 nm [8]. Film thickness can have significant effect in optimizing sensor selectivity and sensitivity [9]. Gas detecting sensitivity also depends on the reactivity of film surface as sensors are strongly influenced by the presence of oxidizing or reducing gases on the surface. The reactivity can be enhanced by impurities, defects and active species on the surface of the films, increasing the adsorption of gas species. It has been shown that inclusion of different doping metals in the oxide films increased the sensitivity to specific gases [10-16]. Gas detection capacity can also be enhanced by mixing metal oxides since each material has its own response and the mixture can add sensitivity and selectivity to specific gas species and also often improves sensor quality and performance [7, 17-19]. An increase of response towards certain gasses has been reported elsewhere, when iron oxide was added into tungsten oxide film [20].

In this paper Electron Beam Evaporation (EBE) process has been used to produce pure and iron-doped tungsten oxide thin films for gas sensor applications. Deposition of tungsten oxide using EBE can produce nanostructured thin film with porosity suitable for gas sensing applications. Whereas the properties of iron-doped tungsten oxide films by EBE for gas sensing applications are not well documented in the literature. In this study physical characterization of pure and iron-doped tungsten oxide thin films have been performed in order to determine the structure of the films, composition, crystallinity and optical properties. Atomic Force Microscopy (AFM) was used to study the surface morphology of

the films. Transmission Electron Microscopy (TEM) was used to investigate the structure of the films. The chemical composition was investigated using X-Ray Photoelectron Spectroscopy (XPS) whereas the crystalline nature of the films was determined using Raman spectroscopy. The optical properties of the films have been characterized using UV-Vis-NIR spectroscopy. Some preliminary gas sensing measurements of the pure and iron-doped tungsten oxide films were performed and reported. Extensive study of the films for gas sensing application will be discussed in another paper.

2. Experimental Methods

2.1. Sample Preparation

Pure and iron (10 at%) incorporated tungsten oxide thin films were produced using electron beam evaporation technique. The films have been deposited on a 12 mm x 12 mm substrate. The substrate was microscopy glass slides. Prior to film deposition the glass substrate was well cleaned with acetone. A 10 mm diameter WO_3 pellet (99.9% purity) and 99.95% purity Fe were used as source targets for evaporation. The WO_3 was first baked in an oven at 800 ^oC for 1 hour in vacuum before used for evaporation to remove any moisture in the material. The electron beam evaporator has dual electron-guns that enable to co-evaporate two materials simultaneously. The WO_3 and Fe targets were placed separately in two copper crucibles that were kept in water-cooled copper hearth of the two electron guns for evaporation. The WO_3 target and Fe were heated by means of an electron beam that have been obtained through heating of tungsten filament cathodes. Two independently power supplies were employed to heat the tungsten filaments. The substrates were placed normal to the evaporation sources at a distance of about 40 cm from the source targets. The

chamber was evacuated to a base pressure of about 1.33 x 10^{-5} Pa to 1.33 x 10^{-4} Pa and an accelerating voltage of about 4 kV was used during evaporation.

During the deposition, film thickness was monitored using two independent quartz crystal monitors for WO_3 and Fe. The metal oxide layer was grown at an average evaporation rate of 1.0 A/s (6 nm/min). The evaporation rate of Fe during co-evaporation with tungsten oxide was about 0.1 A/s (0.6 nm/min). In this paper films of about 200 nm thick have been produced at room temperature. Annealing of the WO_3 and WO_3:F films was performed at 300 ^{o}C for 1 hour in air at a relative humidity of about 30% and the results were compared with the as-deposited films.

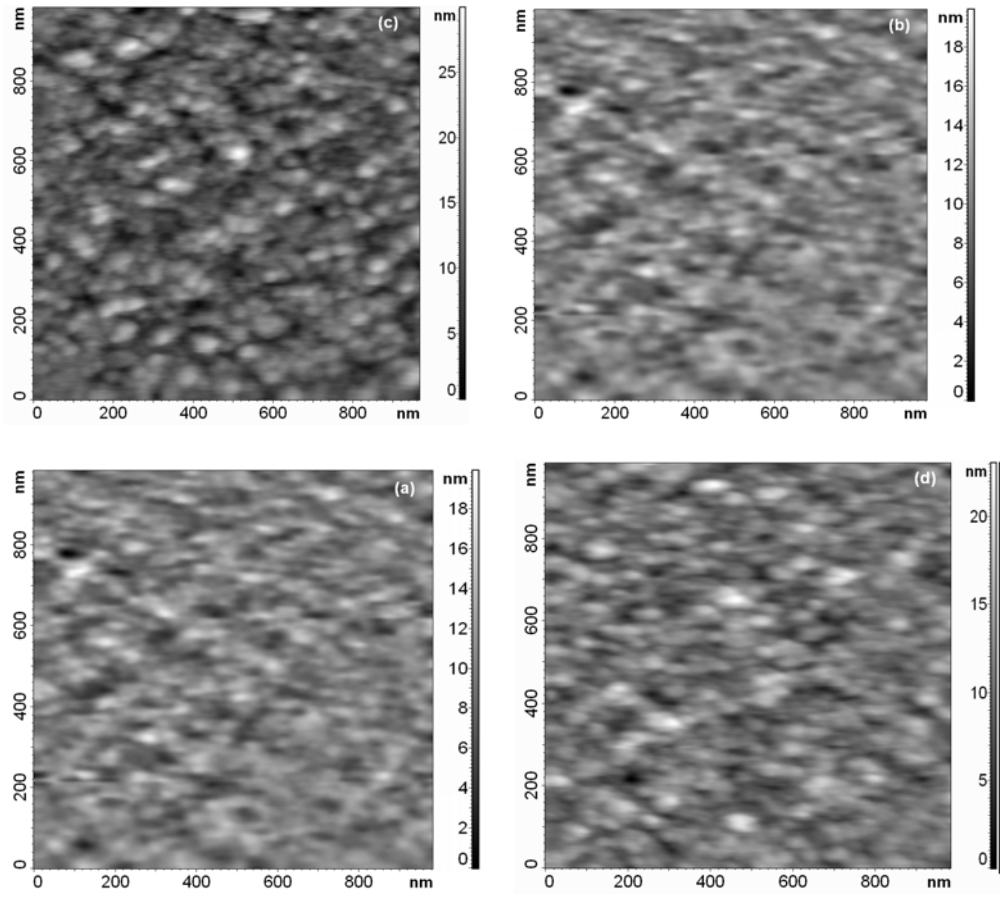

Thin Solid Films, *518 (2010) 4791–4797; doi:10.1016/j.tsf.2010.01.037*.

Figure 1 AFM images of WO_3 and WO_3:Fe films before (a, c) and after (b, d) heat treatment of the samples at 300^{o}C for 1 hour, respectively.

2.2. Sample Characterization

Film thicknesses were performed using *Dekatak* mechanical styles thickness profilometer and the measurements were comparable with the thicknesses obtained form the quartz crystal monitors. AFM images of the film surface were obtained using an NT-MDT Solver P47 scanning probe microscope (NT-MDT Co., Moscow, Russia) with "Golden" Si cantilevers operated in contact mode. A 10 nm diameter tip was used to scan the morphology of the films. The chemical properties of the WO_3 and WO_3:Fe films were determined using X-ray Photoelectron Spectrometer (XPS). Data was acquired using a Kratos Axis ULTRA XPS incorporating a 165 mm hemispherical electron energy analyser. The incident radiation was Monochromatic Al Kα X-rays (1486.6 eV) at 150 W (15 kV, 10 mA) and at 45 degrees to the sample surface. Photoelectron data was collected at take off angle of theta = 90 ^{o}. Survey (wide) scans were taken at an analyser pass energy of 160 eV and multiplex (narrow) high resolution scans at 20 eV. Survey scans were carried out over 1200 - 0 eV binding energy range with 1.0 eV steps and a dwell time of 100 ms. Narrow high-resolution scans were run with 0.05 eV steps and 250 ms dwell time. Base pressure in the analysis chamber was 1.33 x 10^{-7} Pa and during sample analysis 1.33 x 10^{-6} Pa.

Table 1 Average particle diameter and average surface roughness of the WO_3 and WO_3:Fe films obtained using Nova image analysis.

Material	Particle Diameter (nm)	Surface Roughness (nm)

WO_3	-	2.4
WO_3 (annealed)	9	2.6
WO_3:Fe	12	3.2
WO_3:Fe (annealed)	12	2.9

Raman measurements were performed using Renishaw inVia Raman spectrometer to determine the chemical structure and physical state of the film. A Renishaw frequency doubled NdYAG laser excitation source of wavelength 532 nm was used. To avoid local heating of the samples, small power of about 5 mW were applied on the samples. A Raman shift between the wavenumbers 200 to 1200 cm^{-1} has been measured. The reflectance and transmittance of the WO_3 and WO_3:Fe films on glass substrate were measured using PerkinElmer Lambda 900 UV-Visible-NIR spectrophotometer with a 150 mm integrating sphere. The measurements were performed in the wavelength range 300 to 2500 nm at normal angle of incidence. The measured reflectance and transmittance values were subtracted from the base (zero) signal. Teflon coating was used as a 100% reference.

The sensing properties of the WO_3 and WO_3:Fe films were measured to determine the sensing capacity of both films. The resistance and voltage fluctuation across the sensor were measured using noise spectroscopy to characterize the sensitivity and selectivity of the films [21]. Some preliminary results of the films to NH_3 gas at 200 ^oC are shown in this paper.

3. Results and Discussions

3.1. Nanostructure Properties of the Films

Figure 1 shows AFM images of the as-deposited and annealed WO_3 and WO_3:Fe films. Fig. 1a is the micrograph of the as-deposited WO_3 film which displayed the morphology of

amorphous nature. Fig. 1b belongs to the annealed WO_3 film. The film displayed particles with defined boundaries and large porous structure. Fig. 1c-d shows the morphology of the as-deposited and annealed WO_3:Fe films, respectively with slightly promoted particle size but reduced porosity at the surface of both films. The average diameter of the particles and average roughness of the films were estimated using the Nova and Image Analysis software as shown in Table 1. The surface roughness of the WO_3 film increased slightly after annealing. The particle size of the WO_3:Fe film after its heat treatment remained unaltered but its surface roughness decreased slightly (see Table 1). It had been reported earlier that the particle size of WO_3 film was not changed significantly when annealed at temperatures below 300°C [22]. In order to improve the gas-sensing characteristic of a film, optimizations of the particle size and porosity are important factors.

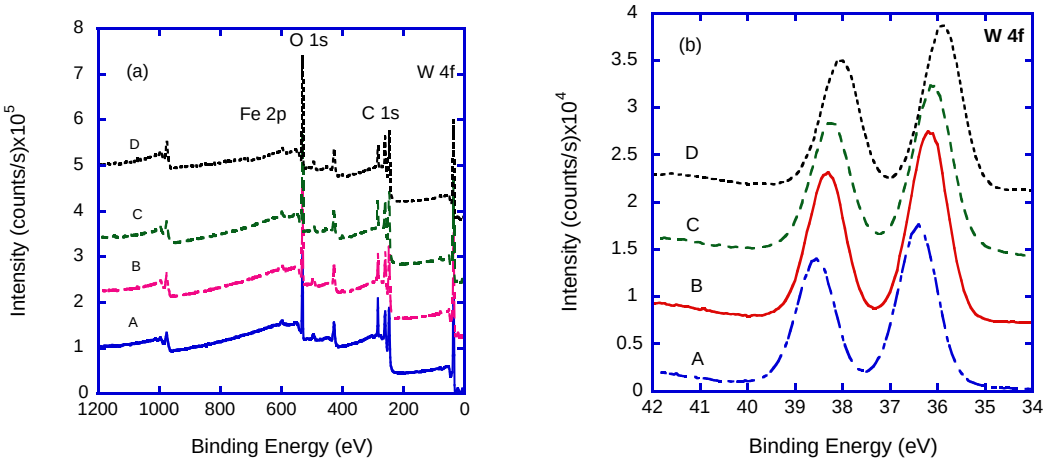

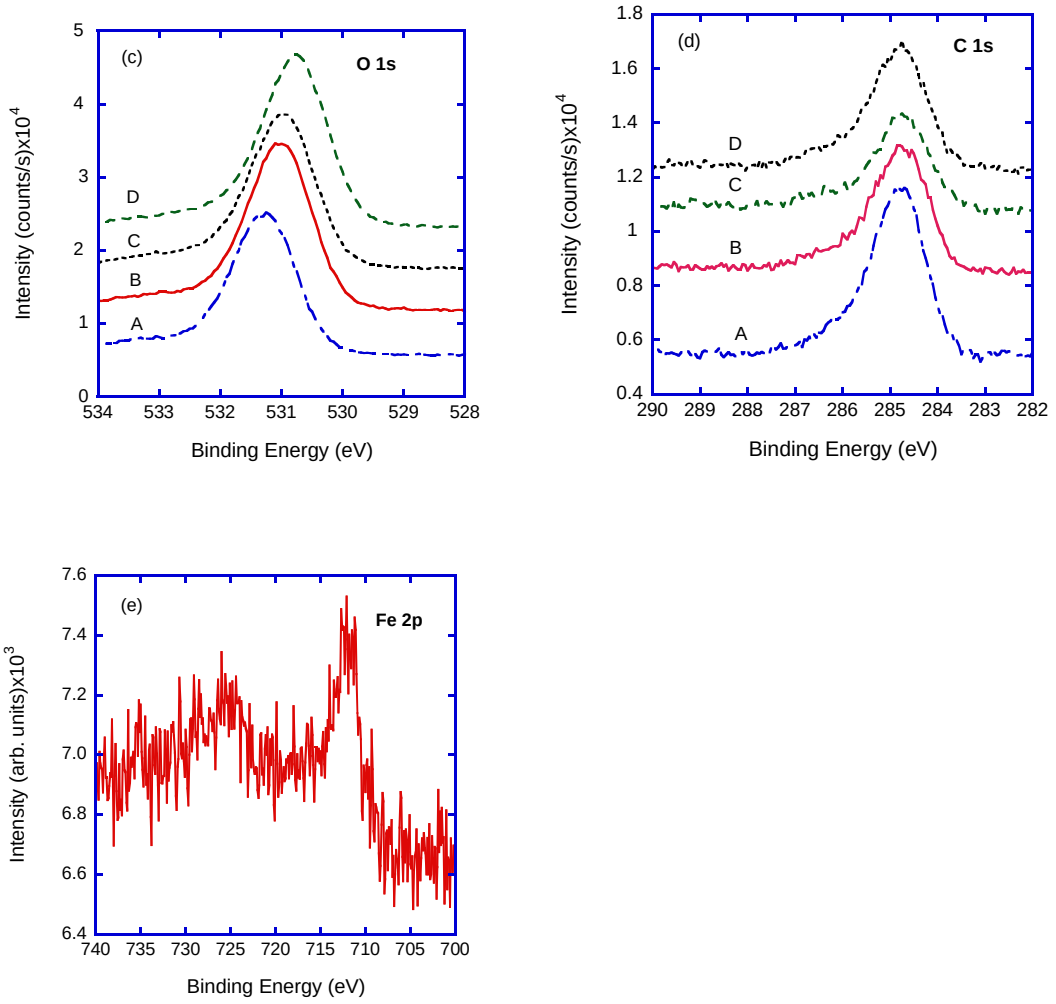

Figure 2 XPS survey (wide) scan of as-deposited and annealed WO_3, and WO_3:Fe films (a), and high resolution spectra of W 4f (b), O1s (c), C 1s (d) and Fe 2p (e). For clarity the spectra A (WO_3), B (annealed WO_3), C (WO_3:Fe) and D (annealed WO_3:Fe) have been shifted vertically.

Table 2 XPS peak positions of W 4f, O 1s, C 1s and Fe 2p obtained from WO_3 and WO_3:Fe films.

Element	Peak Position BE (eV)			
	WO_3	Annealed WO_3	WO_3:Fe	Annealed WO_3:Fe
W 4f	36.4	36.2	36.1	35.9
O 1s	531.2	531.0	531.0	530.8
C 1s	284.8	284.8	284.8	284.8
Fe 2p	-	-	-	712

Thin Solid Films, *518 (2010) 4791–4797; doi:10.1016/j.tsf.2010.01.037*.

Figure 2 shows cross-sectional TEM images of annealed WO_3 and WO_3:Fe films with electron diffraction inserted at the inset of the images. The WO_3:Fe film appears to have a compact microstructure over the entire film as compared to the porous WO_3 film. This looks consistent when compared with the AFM results. Circular reflection rings of electron diffraction patterns of the films were obtained indicating the nanocrystalline nature of the films. The WO_3 also shows discrete electron diffraction patterns.

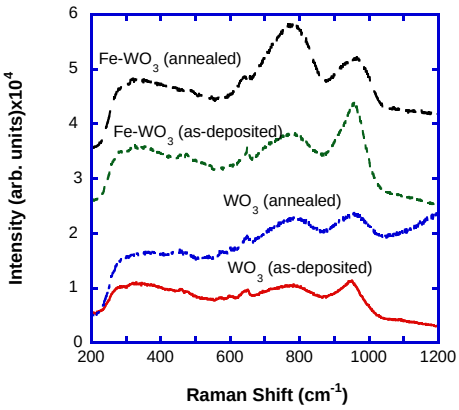

Figure 3 Raman spectra of WO_3 and WO_3:Fe films before and after annealing at 300^{o}C for 1 hour in air measured using 532 nm NdYAG laser source and a power of 5 mW at the sample

3.2. Chemical and Crystalline Nature of the Films

Figure 3 shows X-Ray Photo-electron Spectroscopy (XPS) spectra of the as-deposited and annealed WO_3 and WO_3:Fe films. A general survey of the spectra between binding energies 0 to 1200 eV obtained from scans on the surface of the films are shown in Fig. 3a. From the spectra, photoelectron peaks of W, O and C were observed in all of the films. In addition Fe was detected in very small quantity in the annealed WO_3:Fe film only. From high

resolution spectra the peak positions of W 4f (Fig. 3b), O 1s (Fig. 3c), C 1s (Fig. 3d) and Fe 2p (Fig. 2e) have been determined as shown in Table 2.

The carbon is probably due to the atmospheric contamination and its peak value at binding energy of 284.8 was taken as an energy reference. The core level of W $4f_{5/2}$ and W $4f_{7/2}$ peaks for the as-deposited WO_3 film were measured at binding energies of 38.5 eV and 36.4 eV, respectively. The W $4f_{7/2}$ peak obtained for the as-deposited WO_3 film (36.4 eV) was higher than the fully oxidized WO_3 film reported elsewhere [23, 24]. The W $4f_{5/2}$ and W $4f_{7/2}$ peaks were shifted towards lower energies by 0.2 eV (38.3 eV and 36.2, respectively) when the samples were annealed at 300 ^{o}C for 1 hour. This indicated the improvement of the structure of the film towards stoichiometric equilibrium after heat treatment. The O 1s peaks found at 531.2 eV is characterized as metallic oxides of WO_3. This binding energy of O 1s is shifted to lower energy by 0.2 eV (i.e. 530.0 eV) after heat treatments of the as-deposited sample. Both the W 4f and O 1s core level binding energies shifted by the same amount and this is most likely a shift of Fermi level [25]. Similarly the W $4f_{5/2}$ and W $4f_{7/2}$ core levels of the as-deposited WO_3:Fe film found at 38.2 eV and 36.1 eV were shifted by 0.2 eV (38.0 eV and 35.9 eV, respectively) when annealed the film at 300^{o}C for 1 hour. The Fe 2p spectrum of the annealed WO_3:Fe (Fig. 2e) contains a broader peak of iron oxides which resulted from Fe^{+3} species [20].

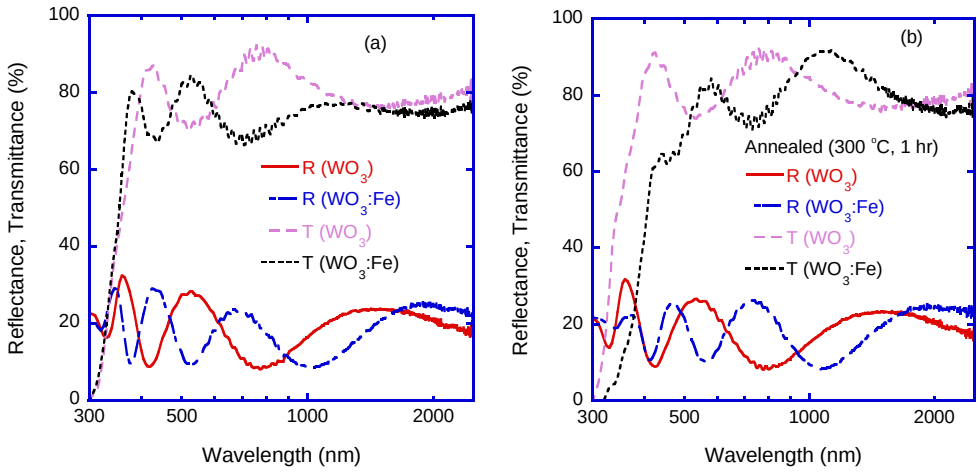

Figure 4 Transmittance and reflectance as a function of wavelength between 300 nm to 2500 nm of (a) WO_3 film and (b) WO_3:Fe film. Spectra of both the as-deposited and annealed samples are shown.

Raman spectroscopy was employed to characterize the chemical and crystalline nature of the WO_3 and WO_3:F thin films as both films were found to be amorphous at grazing incidence X-ray Diffraction measurements [24]. From Figure 3, the as-deposited WO_3 film has a week and broad Raman peaks around 951 cm^{-1} and 775 cm^{-1}. These features are characteristic of amorphous materials assigned to the stretching frequency modes of the bridging oxygen W=O and O-W-O, respectively [26]. Raman peaks of the annealed sample were slightly blue-shifted with peak positions at about 957 cm^{-1} and 779 cm^{-1}, respectively. The addition of Fe to WO_3 seems to prompt an increase in particle size and probably induced the formation of little crystallization of the WO_3 film, as can be seen from the Raman intensity. From AFM it was observed a slight increase of particle size after annealing the film. The high (low) Raman frequency modes around the wavenumber 950 cm^{-1} (770 cm^{-1}) decreased (increased) in intensity when the particle size increases. This

could be due to vibrations of surface atoms which become comparable in number with volume atoms for small size crystallites.

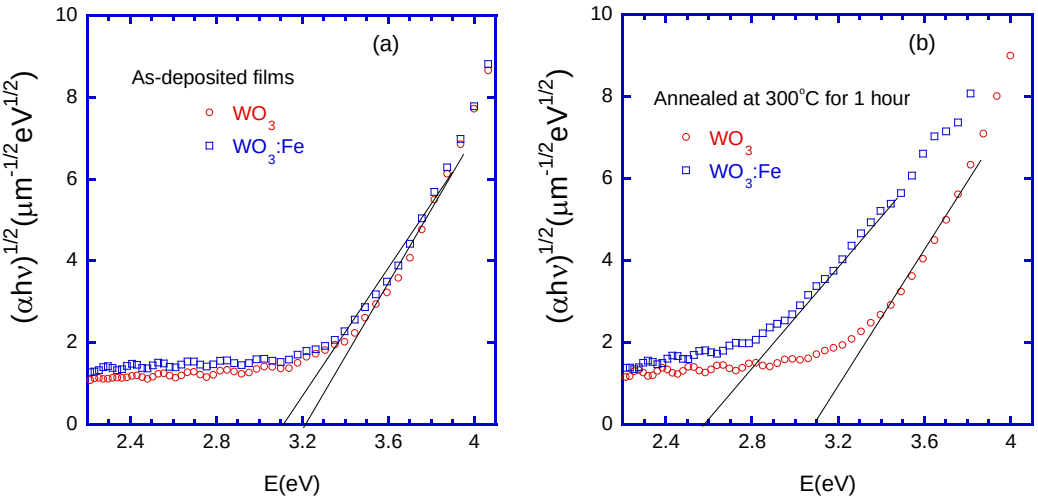

Figure 5 Tauc plot showing $(\alpha h\nu)^{1/2}$ vs E=hν of (a) WO_3, and (b) WO_3:Fe films before and after annealing.

3.3. Optical Properties of the Films

Optical properties of tungsten oxide films were measured in the solar wavelength range between 300 nm and 2500 nm. Figure 4a-b shows the transmittance and reflectance of 200 nm thick WO_3 film and 225 nm thick WO_3:Fe film before and after heat treatments. From the figures, the on-set of transmittance for the WO_3 film increases sharply as compared to the WO_3:Fe film. After annealing the samples at 300°C for 1 hour, the optical transition wavelengths were slightly shifted towards higher wavelength. Solar and luminous transmittance and reflectance of the films were determined by weighting the transmittance and reflectance of the films to the intensity of the corresponding solar and visible spectrum

for air mass 1.5 as shown in Table 3. The WO_3 film is found to be fairly transparent in excess of 80% in its solar transmittance.

The optical absorption coefficient (α) of the as-deposited and annealed WO_3 and WO_3:Fe films were calculated from the reflectance (R) and transmittance (T) measurements and the thickness of the film (*d*) using the relationship found elsewhere [27]:

$$\alpha d = \ln\left(\frac{1-R}{T}\right) \quad (1)$$

The band gap energy (E_g) of the films was determined from the following relationship which is know as Tauc plot [28]:

$$\alpha h\upsilon = c(h\nu - E_g)^n \quad (2)$$

where h□ is the incident photon energy, c is a constant and *n* is an exponent and has the value of 2 for an indirect transition. As shown in Figure 5, extrapolation of the straight line curves along the energy gives an estimation of optical band gap energy of 3.22 eV and 3.12 eV for the WO_3 and WO_3:Fe, respectively. This showed a slight decrease of the band gap energy when iron was incorporate into the WO_3 film [29]. Furthermore, the E_g of the annealed samples were found to have lower values (WO_3=3.12 eV and WO_3:Fe=2.61 eV) as compared to the corresponding E_g values of the as-deposited films. The reduction of E_g after the annealing treatment can be related to the state of formation of crystallization of the film. Narrowing of band gap due to increasing crystallite size in sputtered WO_3 films has been previously observed [30]. The optical band gap energies of the as-deposited (3.22 eV) and annealed WO_3 (3.12 eV) films obtained in this paper are found to be within the ranges

of bang gap energy of WO_3 thin films deposited by various methods reported elsewhere [2, 31, 32].

Table 3 Solar and luminous transmittance of WO_3 and WO_3:Fe films before and after annealing at 300^{o}C for 1 hour.

	Film Thickness	T-sol (%)	T-vis (%)	R-sol (%)	R-vis (%)
WO_3	200 nm	82	76	18	24
WO_3 (annealed)	200 nm	80	74	18	25
WO_3:Fe	225 nm	73	79	17	14
WO_3:F (annealed)	225 nm	75	78	18	14

3.4. Gas Sensing Properties of the Films

Preliminary results indicated that the tungsten oxide film was found to be sensitive to various toxic gasses. Figure 6 is an example of WO_3 sensor exposed to 10 ppm NH_3 gas at 200^{o}C for different times between 3 to 15 minutes as measured using noise spectroscopy. Saturation of the detected power density signal (PDS) occurred after 10 minutes of exposure to NH_3 gas and this indicated a fast response of the film. Synthetic air was used as a reference. The gas sensing measurements technique and results of the tungsten oxide as a gas sensor to various gasses at various temperatures will be discussed in another paper.

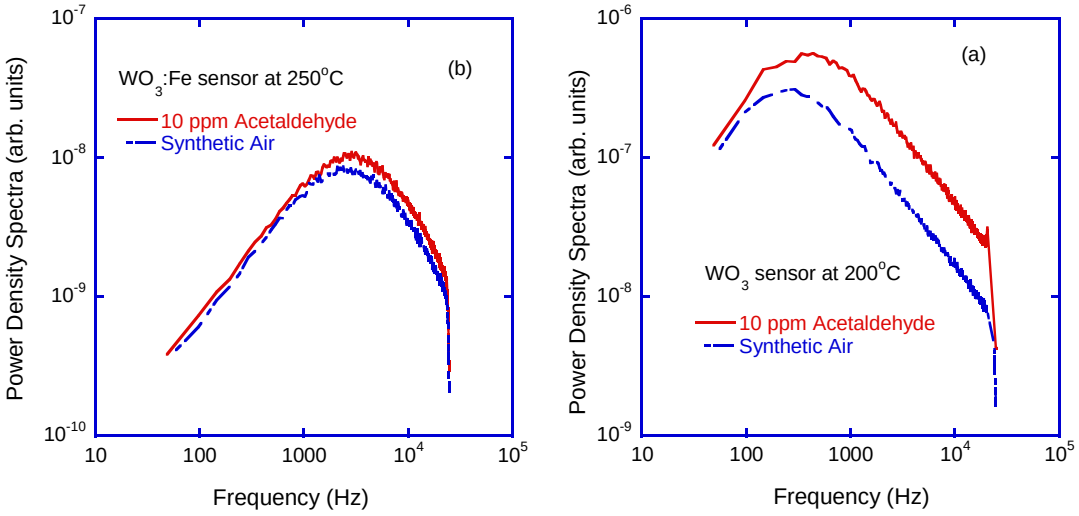

Figure 6 Power Density Spectra (PDS) of WO_3 sensor exposed to 10 ppm NH_3 at 200°C for different times between 3 to 15 minutes.

4. **Conclusions**

Thin films of WO_3 and WO_3:Fe have been developed using electron beam evaporation process. The physical properties of the films have been investigated using various techniques. The as-deposited WO_3 films have shown very fine nanostructured particles with amorphous behavior. Annealing of the film at 300°C and/or addition of Fe into the film promoted a slight increase of the particle size. The films have shown significant amount of porosity and a nearly stoichiometric properties with optical band-gap energies within the UV/Vis part of the solar spectrum ranging between 0.38 □m to 0.45 □m. The results are found to be suitable for gas sensor application which is also evident from the preliminary results. Gas sensing properties of pure and iron incorporated tungsten oxide film will be reported in another paper.

Acknowledgements

Thin Solid Films, *518 (2010) 4791–4797; doi:10.1016/j.tsf.2010.01.037*.

The first author is indebt to the Japanese Society for the Promotion of Science (JSPS) for the financial assistance to perform experiment at Hokkaido University in Sapporo. This research was done during Professional Development Leave offered to the first author by Queensland University of Technology.

References

[1] C. Cantalini, H.T. Sun, M. Faccio, M. Pelino, S. Santucci, L. Lozzi, M. Passacantando, Sensors and Actuators B: Chemical Materials for Sensors 31/1-2 (1996) 81.
[2] R. Sivakumar, M. Jayachandran, C. Sanjeeviraja, Materials Chemistry and Physics 87/2-3 (2004) 439.
[3] T. Siciliano, A. Tepore, G. Micocci, A. Serra, D. Manno, E. Filippo, Sensors and Actuators B: Chemical 133/1 (2008) 321.
[4] Y.-G. Choi, G. Sakai, K. Shimanoe, N. Miura, N. Yamazoe, Sensors and Actuators B: Chemical 95/1-3 (2003) 258.
[5] A. Hoel, L.F. Reyes, P. Heszler, V. Lantto, C.G. Granqvist, Current Applied Physics 4/5 (2004) 547.
[6] S.-K. Song, J.-S. Cho, W.-K. Choi, H.-J. Jung, D. Choi, J.-Y. Lee, H.-K. Baik, S.-K. Koh, Sensors and Actuators B: Chemical 46/1 (1998) 42.
[7] M. Stankova, X. Vilanova, J. Calderer, E. Llobet, J. Brezmes, I. Gràcia, C. Cané, X. Correig, Sensors and Actuators B: Chemical 113/1 (2006) 241.
[8] X. Wang, S.S. Yee, W.P. Carey, Sensors and Actuators B: Chemical 25/1-3 (1995) 454.
[9] G.G. Mandayo, E. Castaño, F.J. Gracia, A. Cirera, A. Cornet, J.R. Morante, Sensors and Actuators B: Chemical 95/1-3 (2003) 90.
[10] H. Kawasaki, T. Ueda, Y. Suda, T. Ohshima, Sensors and Actuators B: Chemical 100/1-2 (2004) 266.
[11] V. Khatko, E. Llobet, X. Vilanova, J. Brezmes, J. Hubalek, K. Malysz, X. Correig, Sensors and Actuators B: Chemical 111-112 (2005) 45.
[12] L.J. LeGore, R.J. Lad, S.C. Moulzolf, J.F. Vetelino, B.G. Frederick, E.A. Kenik, Thin Solid Films 406/1-2 (2002) 79.
[13] M.A. Ponce, C.M. Aldao, M.S. Castro, Journal of the European Ceramic Society 23/12 (2003) 2105.
[14] J. Shieh, H.M. Feng, M.H. Hon, H.Y. Juang, Sensors and Actuators B: Chemical 86/1 (2002) 75.
[15] A. Rothschild, F. Edelman, Y. Komem, F. Cosandey, Sensors and Actuators B: Chemical 67/3 (2000) 282.
[16] D.H. Yoon, G.M. Choi, Sensors and Actuators B: Chemical 45/3 (1997) 251.

[17] L.E. Depero, I. Natali Sora, C. Perego, L. Sangaletti, G. Sberveglieri, Sensors and Actuators B: Chemical Materials for Sensors: Functional Nanoscaled Structures of the 1995 E-MRS Spring Conference 31/1-2 (1996) 19.
[18] K. Zakrzewska, Vacuum Proceedings of the International Workshop on Surface Physics: Metals on Solid Surfaces 74/2 (2004) 335.
[19] G. Neri, A. Bonavita, G. Rizzo, S. Galvagno, N. Pinna, M. Niederberger, S. Capone, P. Siciliano, Sensors and Actuators B: Chemical 122/2 (2007) 564.
[20] E. Comini, L. Pandolfi, S. Kaciulis, G. Faglia, G. Sberveglieri, Sensors and Actuators B: Chemical 127/1 (2007) 22.
[21] J.S. Bendat, A.G. Piersil, Random Data Analysis and Measurment Procedures, Wiley, New York, USA, 2000.
[22] R. Sivakumar, R. Gopalakrishnan, M. Jayachandran, C. Sanjeeviraja, Optical Materials 29/6 (2007) 679.
[23] L. Lozzi, L. Ottaviano, M. Passacantando, S. Santucci, C. Cantalini, Thin Solid Films 391/2 (2001) 224.
[24] D. Gogova, L.K. Thomas, B. Camin, Thin Solid Films 517/11 (2009) 3326.
[25] T.G.G. Maffeis, D. Yung, L. LePennec, M.W. Penny, R.J. Cobley, E. Comini, G. Sberveglieri, S.P. Wilks, Surface Science 601/21 (2007) 4953.
[26] A. Cremonesi, Y. Djaoued, D. Bersani, P.P. Lottici, Thin Solid Films 516/12 (2008) 4128.
[27] R. Boucher, Journal of Physics and Chemistry of Solids 66/5 (2005) 906.
[28] J. Tauc, Amorphous and Liquid Semiconductors Plenum Press, London 1974.
[29] A.Z. Moshfegh, R. Azimirad, O. Akhavan, Thin Solid Films 484/1-2 (2005) 124.
[30] C.G. Granqvist, Handbook of Inorganic Electrochromic Materials, Elsevier, Amsterdam, 1995.
[31] L.G. Teoh, J. Shieh, W.H. Lai, I.M. Hung, J. Alloys Compd. 396 (2005) 251.
[32] A. Rougier, F. Portemer, A. Quédé, M. El Marssi, Applied Surface Science 153/1 (1999) 1.